

TWO OPTICAL COUNTERPART CANDIDATES OF M82 X-1 FROM HST OBSERVATIONS

SONG WANG¹, JIFENG LIU¹, YU BAI¹, AND JINCHENG GUO^{1,2}*Draft version December 21, 2021*

ABSTRACT

Optical counterparts can provide significant constraints on the physical nature of ultraluminous X-ray sources (ULXs). In this letter, we identify six point sources in the error circle of a ULX in M82, namely M82 X-1, by registering *Chandra* positions onto *Hubble Space Telescope* images. Two objects are considered as optical counterpart candidates of M82 X-1, which show F658N flux excess compared to the optical continuum that may suggest the existence of an accretion disk. The spectral energy distributions of the two candidates match well with the spectra for supergiants, with stellar types as F5-G0 and B5-G0, respectively. Deep spatially resolved spectroscopic follow-up and detailed studies are needed to identify the true companion and confirm the properties of this BH system.

Subject headings: galaxies: individual (M82) — X-rays: binaries — black hole physics

1. INTRODUCTION

Ultraluminous X-ray sources (ULXs) are extranuclear sources with an observed luminosity in excess of 10^{39} erg/s, which are possibly the long-sought intermediate mass black holes (IMBHs), or stellar mass black holes (SMBHs) in a new ultraluminous accretion state (Gladstone et al. 2009). M82 X-1 is one of the most promising IMBH candidates based on multiple X-ray properties: the extremely high luminosities (Matsumoto et al. 2001; Kaaret et al. 2006b), the quasi-periodic oscillation (QPO) behaviors in the 0.05–0.1 Hz frequency range (Strohmayer & Mushotzky 2003; Feng & Kaaret 2007), the new-identified thermally dominant states (Feng & Kaaret 2010), and a 3:2 QPO at frequencies of 3.32 and 5.07 Hz (Pasham et al. 2014), all of which point to an IMBH of several hundred solar masses or above, although some models (Okajima et al. 2006) suggested M82 X-1 may be a massive SMBH ($19\text{--}32 M_{\odot}$) shining at a super-Eddington luminosity.

The optical counterpart may provide crucial diagnostics about the nature of one ULX. The magnitudes and colors of the optical counterpart may help reveal the type of the donor star and distinguish between SMBHs and IMBHs (Madhusudhan et al. 2008), while optical spectroscopic monitoring can be used to obtain dynamical mass estimates for the BH system (Liu et al. 2013). Many efforts have been done to search for the optical counterpart of M82 X-1, which was first reported to be associated with a young massive star cluster MGG 11 (Portegies Zwart et al. 2004). However, with more careful astrometry from *HST* Near Infrared Camera and Multi-Object Spectrometer (NICMOS) and Wide Field Camera 3 (WFC3)/Infrared Channel images, Kong et al. (2007) and Voss et al. (2011) argued that M82 X-1 is ~ 0.65 arcsec away from MGG 11, with an offset significance of 3σ . Using archive images obtained by the Second Wide Field and Planetary Camera, no optical counterpart was found for M82 X-1 (Ptak et al. 2006).

Recently, Gladstone et al. (2013) reported two candidate counterparts of M82 X-1 using the Advanced Camera for Surveys (ACS)/Wide Field Camera (WFC) observations, however, both of them are resolved into several sources in the images of ACS/High Resolution Camera (HRC). Motivated by these studies presented above, we decide to obtain more precise location of the optical counterpart for follow-up studies on M82 X-1.

In this letter, we reexamine the *HST* data to perform accurate astrometry and photometry for M82 X-1. Two candidate optical counterparts of M82 X-1 are identified, and some constraints on their physical nature are discussed from the multiband spectral energy distribution (SED). We describe our data analysis and results in Section 2, and present SEDs for the counterparts in Section 3. A discussion follows in Section 4.

2. DATA ANALYSIS AND RESULTS

2.1. Astrometry

For precise localization of M82 X-1 on optical images, we use multiple matched pairs of objects between *Chandra* and *HST* observations with the help of Sloan Digital Sky Survey (SDSS) observations. For the *Chandra* image, we select one of the deepest ACIS observations (Obsid 10543), and used the CIAO tool WAVDETECT to detect X-ray sources. Xu et al. (2015) provided X-ray position for M82 X-1 (R.A.=9:55:50.123, decl.=+69:40:46.54) using the same observation, which is adopted as the original *Chandra* position of the ULX. The region around M82 X-1 has been observed frequently with *HST* using ACS, including HRC and WFC, and WFC3/Ultraviolet-Visible Channel (UVIS). Here the ACS/WFC F555W observation (Data Set j9l021d8q) is selected for the wide field of view ($\sim 202'' \times 202''$). The observation from SDSS Data Release 12 is used for intermediate comparisons, because it is hard to find matches that can be used for a direct registration of *Chandra* and *HST* images (Voss et al. 2011). The matched pairs of objects in the comparisons are presented in Table 1. The astrometric errors for the SDSS-*Chandra* and SDSS-*HST* comparisons are $0.44''$ and $0.18''$ in right ascension, while $0.33''$ and $0.02''$ in declination. The final correction used to translate the *Chandra* position of M82 X-1

¹ Key Laboratory of Optical Astronomy, National Astronomical Observatories, Chinese Academy of Sciences, Beijing 100012, China; jfliu@bao.ac.cn, songw@bao.ac.cn

² University of Chinese Academy of Sciences, Beijing 100049, China

onto the *HST* image is $1.74'' \pm 0.48''$ in right ascension and $0.30'' \pm 0.33''$ in declination. The uncertainties are a quadratic sum of the standard deviations of these comparisons.

To better resolve the objects in the crowded region around M82 X-1, the observations from ACS/HRC, with a higher spatial resolution than that of ACS/WFC, are scrutinized. As shown in Fig. 1, M82 X-1 is located beyond the super star cluster MGG 11, and there are six point sources (A to F) located inside the $0.4''$ error circle, which is the equivalent radius ($\sim \sqrt{0.48'' \times 0.33''}$) of its error ellipse. No other point sources are detected with IRAF/DAOFIND or DOLPHOT³. Among the six objects, source A lies closest to the regional center of M82 X-1 ($\Delta r \approx 0.096''$). Source C and F is the reddest and bluest one, respectively. The two optical counterpart candidates identified by Gladstone et al. (2013) are shown with green diamonds, both of which are resolved into several sources by virtue of the high spatial resolution of ACS/HRC. Although one of these is located inside the $0.4''$ circle, it is quite extended, and is not considered as a counterpart.

2.2. Photometry

Aperture photometry for the six sources is performed with a small aperture radius ($0.05''$) to avoid contamination from nearby objects in this crowded region. A small annulus immediately surrounding each source, with inner radius as $0.06''$ and outer radius as $0.08''$, is adopted to obtain the background intensity, considering that these sources are superimposed onto a bright and variable background. The photometry is performed using the DAOPHOT package in IRAF on drizzled images produced from *HST* standard pipeline calibration. The WREGISTER package in IRAF is used to align the frames in the same observation sequence. For example, all the 16 WFC images in 2006 year are aligned to j9l024dtq_drz.fits. A bright nearby star is used to correct the positions of the six objects for observations in different sequences. Although photometry with point-spread function (PSF) fitting is more robust than aperture photometry in dense environments, the six objects are so faint that the flux profiles are poorly fit with the PSF. The PSF-fitting package DOLPHOT is experimented to derive photometry, but the results are poor and unacceptable. Therefore, only the results from DAOPHOT are presented here.

The Vega magnitude zero points (ZPTs) are then adopted to compute the *HST* filter-dependent Vega magnitudes for each source. For ACS observations, the ZPTs referring to an “infinite” radius are taken from Sirianni et al. (2005). For WFC3 data, the ZPTs corresponding to a $0.4''$ radius aperture are taken from the WFC3 Data Handbook. We then derive the point-spread function models from Tiny Tim⁴, and determine the aperture corrections from the $0.05''$ radius aperture to the $0.5''$ (ACS) or $0.4''$ (WFC3) radius aperture using these models. For ACS data, additional corrections from a $0.5''$ radius to an “infinite” radius are taken (Sirianni et al. 2005).

The *HST* observations and computed magnitudes for the six sources are listed in Table 2. The magnitude uncertainty only includes the error in the aperture sum, while the error due to background is not included, the latter of which is considered as a statistical effect. It should be noted that there are some variations in the photometry between different frames of the same exposure sequence (e.g., the four WFC/F435W images observed in 2006 year), and the variations can reach even one mag in some cases. In order to check the photometry accuracy, new photometry is performed on the *HST* observations with astrometric offsets corrected by TweakReg⁵. The test gives approximate photometry results, indicating the variations among these exposures are real. In addition, some photometry are performed for several small regions near these sources to check the background fluctuations. Similar variations between different frames of the same exposure sequence are found for these background regions, suggesting these variations are mostly caused by background fluctuations that would influence the photometry of faint objects, rather than being short-term variabilities of these point sources. This is not surprising, given the substantial and extensive diffuse emission in the nuclear starburst region of M82 (McCraday et al. 2003).

3. SED OF THE COUNTERPARTS

Spectral energy distributions for these six objects are constructed from *HST* photometry, and two examples (object A and F) are plotted in Fig. 2. The SED of a nearby super star cluster MGG 6 is overplotted for comparison, which shows a much steeper trend towards the red band due to numbers of dwarf stars; the red band of object A and F, like stellar objects, is much flatter. The SED of MGG 6 displays much brighter magnitudes ($F814W \approx 17$ mag) and redder colors than all the six objects. Quantitatively, the mean color $F814W_{\text{HRC}} - F550M_{\text{HRC}}$ for the six objects is 2.2 mag, while $F814W_{\text{HRC}} - F550M_{\text{HRC}} = 3.5$ mag for MGG 6. Although no exact intrinsic color can be obtained without accurate extinction, such notable differences suggest that these six objects are likely stellar objects instead of super star clusters.

To classify the counterparts, SED templates are calculated with the SYNPHOT tool CALCSPEC using the CK04 standard stellar spectra (Castelli & Kurucz 2004) with solar metallicity. All SED templates are normalized to a *V*-band magnitude of zero for simple comparisons. The standard stars in the CK04 models, whose absolute magnitudes are taken from Schmidt-Kaler (1982) and Martins et al. (2005), are placed at the distance of M82 (3.63 Mpc; Freedman et al. 1994). Assuming Galactic relation $N_{\text{H}} = 5.8 \times 10^{21} E(B - V)$ (Bohlin et al. 1978), the extinction toward M82 X-1 is calculated as $E(B - V) \simeq 1.9$, with $N_{\text{H}} \simeq 1.1 \times 10^{22} \text{ cm}^{-2}$ inferred from the X-ray spectrum of the ULX (Feng & Kaaret 2010). Note that, the X-ray based N_{H} absorption may include contribution from the accretion disk itself, which may have little effect on the optical observation of the secondary, thus a lower extinction is possible for the secondary. In the following analysis, variable $E(B - V)$

³ <http://americano.dolphinsim.com/dolphot/>

⁴ <http://tinytim.stsci.edu/cgi-bin/tinytimweb.cgi>.

⁵ http://ssb.stsci.edu/doc/stsci_python_dev/drizzlepac.doc/html/tweakreg.html

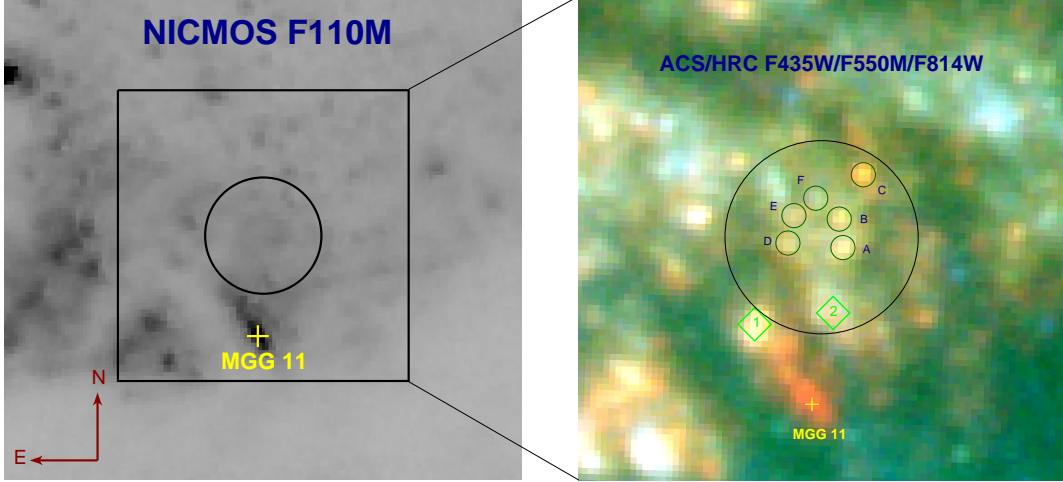


FIG. 1.— Left panel: The *HST* NICMOS image around M82 X-1. The $0.4''$ circle shows the corrected X-ray position, and the box shows a region of $2'' \times 2''$. The plus marks the position of the super star cluster MGG 11. Right Panel: False-color ACS/HRC map around M81 X-1, using the F435W (blue), F550M (green), and F814W (red). The six small circles, with radii of $0.05''$, represent six point sources located inside of the $0.4''$ circle. The green diamonds show the two candidate counterparts identified by Gladstone et al. (2013), both of which have been resolved into several sources due to the high resolution of ACS/HRC.

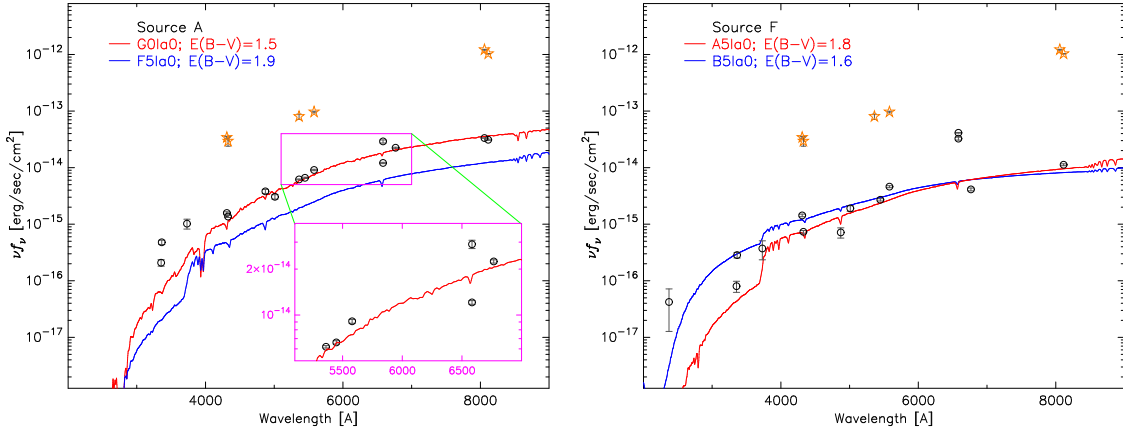


FIG. 2.— Left panel: The SED of source A. The black circles represent the apparent magnitudes of source A, while the stars represent the magnitudes of a nearby super star cluster MGG 6. A mean magnitude is plotted for observations with the same detector and filter. The red and blue line represent the spectra of a supergiant G0 Ia0 ($M_V = -8.9$) and F5 Ia0 ($M_V = -9.0$), with different extinction correction, respectively. Right panel: The SED of source F. The black circles represent the apparent magnitudes of source F, and the stars indicate the SED of MGG 6. The red and blue line represent the spectra of a supergiant A5 Ia0 ($M_V = -8.8$) and B5 Ia0 ($M_V = -8.4$), with different extinction correction, respectively.

values ranging from 1.0 to 1.9 are adopted in comparing the observed SEDs and the templates (from O to M).

The red part ($\lambda > 4000 \text{ \AA}$) of the observed SEDs and the templates are used for the comparison, since the blue emission of an X-ray binary may be contaminated by emission from the accretion disk and reprocessed emission from an X-ray illuminated accretion disk or stellar surface (Tao et al. 2011), the last of which could brighten the system by up to ~ 5 mag (Copperwheat et al. 2007). With simple comparisons, the SEDs of sources A, B, C, D, E, and F match well with those of supergiants, with types as F5-G0, A0-F5, K5-M0, A5-F5, F0-F5, and B5-G0, respectively. Here no exact fitting is done in the comparison, because the extinction can vary in a wide range. It should be noted that the wide range of the spectral type for each source is due to the wide range of the extinction.

4. DISCUSSION

In this work, we have carried out careful relative astrometry and identified six objects in the immediate region around M82 X-1, and also estimated their types from their observed SEDs constructed from *HST* photometry.

Intriguingly, both source A (in Data Set j8mx19010 and j9fb09030) and F (in all observations) show excessive fluxes relative to the optical continuum in the narrow H_α filter F658N. Note that the background intensity has been carefully subtracted, and there is no F658N flux excess in the SEDs of other nearby sources (B, C, D, and E). Generally, H_α emission can come from H II regions, planetary nebulae, or accretion disks. Both H II regions and planetary nebulae produce significant S II (6731 \AA) emission in the narrow S II filter F673N along with H_α emission, yet no excessive S II emission is seen in the F673N observations for any of the objects. This suggests

that the H_α emission of source A and F does not come from H II regions or planetary nebulae, but is likely produced by an accretion disk, hence suggesting that one of the two sources is the optical counterpart of M82 X-1.

For source A, the blue part of the SED is brighter than that of a late-type companion star, suggesting that the blue component may come from combined emission of the companion star and the accretion disk, while the red component may come mainly from the companion star. Except for source A, the other five objects do not show clear blue excess in the SEDs. Source F is the bluest one among the six objects, and is hardly seen in the F814W images. This may suggest the blue emission comes from an accretion disk, as some studies (Pakull et al. 2006; Tao et al. 2011) have claimed the dominant component of optical emission in most ULXs is produced through X-ray irradiation of the outer accretion disk. Sources F, D and E exhibit variability in multiple observations, however, the crowded environments and bright background restrain us from confirming whether the long-term flux variability is real. In addition, sources D and E seem a little more extended than other four objects, but the SEDs indicate they could not be star clusters or peaks in the diffuse emission (no feature of H II region).

The scenario of a supergiant companion is consistent with the orbital period of 62 days of M82 X-1, and the short phase with Roche lobe overflowing indicates M82 X-1 is in a brief and unusual period of its evolution (Kaaret et al. 2006a). Further deep spatially resolved spectroscopic observation would provide more information on the two candidates, and unveil the nature of M82 X-1.

We especially thank the anonymous referee for his/her thorough report and helpful comments and suggestions that have significantly improved the paper. This work is based on observations made with the NASA/ESA *Hubble Space Telescope*, obtained from the Mikulski Archive for Space Telescopes. Some of the data presented in this paper were obtained from the *Chandra* Data Archive and SDSS-III. The authors acknowledge support from the National Science Foundation of China under grants NSFC-11273028 and NSFC-11333004, and support from the National Astronomical Observatories, Chinese Academy of Sciences under the Young Researcher Grant.

REFERENCES

- Bohlin, R. C., Savage, B. D., & Drake, J. F. 1978, *ApJ*, 224, 132
 Castelli, F., & Kurucz, R. L. 2004, arXiv:astro-ph/0405087
 Copperwheat, C., Cropper, M., Soria, R., & Wu, K. 2007, *MNRAS*, 376, 1407
 Feng, H., & Kaaret, P. 2007, *ApJ*, 668, 941
 Feng, H., & Kaaret, P. 2010, *ApJL*, 712, L169
 Freedman, W. L., Hughes, S. M., Madore, B. F., et al. 1994, *ApJ*, 427, 628
 Gladstone, J. C., Copperwheat, C., Heinke, C. O., et al. 2013, *ApJS*, 206, 14
 Gladstone, J. C., Roberts, T. P., & Done, C. 2009, *MNRAS*, 397, 1836
 Kaaret, P., Simet, M. G., & Lang, C. C. 2006a, *ApJ*, 646, 174
 Kaaret, P., Simet, M. G., & Lang, C. C. 2006b, *Science*, 311, 491
 Kong, A. K. H., Yang, Y. J., Hsieh, P.-Y., Mak, D. S. Y., & Pun, C. S. J. 2007, *ApJ*, 671, 349
 Liu, J.-F., Bregman, J. N., Bai, Y., Justham, S., & Crowther, P. 2013, *Nature*, 503, 500
 Madhusudhan, N., Rappaport, S., Podsiadlowski, P., & Nelson, L. 2008, *ApJ*, 688, 1235
 Martins, F., Schaerer, D., & Hillier, D. J. 2005, *A&A*, 436, 1049
 Matsumoto, H., Tsuru, T. G., Koyama, K., et al. 2001, *ApJL*, 547, L25
 McCrady, N., Gilbert, A. M., & Graham, J. R. 2003, *ApJ*, 596, 240
 Okajima, T., Ebisawa, K., & Kawaguchi, T. 2006, *ApJL*, 652, L105
 Pakull, M. W., Grisé, F., & Motch, C. 2006, *Populations of High Energy Sources in Galaxies*, 230, 293
 Pasham, D. R., Strohmayer, T. E., & Mushotzky, R. F. 2014, *Nature*, 513, 74
 Portegies Zwart, S. F., Baumgardt, H., Hut, P., Makino, J., & McMillan, S. L. W. 2004, *Nature*, 428, 724
 Ptak, A., Colbert, E., van der Marel, R. P., et al. 2006, *ApJS*, 166, 154
 Schmidt-Kaler, Th. 1982, in *Numerical Data and Functional Relationships in Science and Technology Vol. 2b: Stars and Star Clusters*, ed. K. Schaifers & H. H. Voigt (Berlin: Springer), 15
 Sirianni, M., Jee, M. J., Benítez, N., et al. 2005, *PASP*, 117, 1049
 Strohmayer, T. E., & Mushotzky, R. F. 2003, *ApJL*, 586, L61
 Tao, L., Feng, H., Grisé, F., & Kaaret, P. 2011, *ApJ*, 737, 81
 Xu, X.-j., Liu, J., & Liu, J. 2015, *ApJL*, 799, L28
 Voss, R., Nielsen, M. T. B., Nelemans, G., Fraser, M., & Smartt, S. J. 2011, *MNRAS*, 418, L124

TABLE 1
POSITIONS OF SOURCES FOR *Chandra*-SDSS AND SDSS-*HST* ASTROMETRIC REGISTRATION.

Bright <i>Chandra</i> ACIS X-ray Sources identified in SDSS Observations				
<i>Chandra</i> R.A.	<i>Chandra</i> Decl.	SDSS R.A.	SDSS Decl.	Displacement (")
9:56:58.658	+69:38:52.12	9:56:58.670	+69:38:52.53	0.423
9:55:43.066	+69:34:55.20	9:55:43.018	+69:34:54.82	0.461
9:55:05.222	+69:44:42.47	9:55:05.182	+69:44:42.48	0.220
9:55:14.585	+69:47:35.59	9:55:14.530	+69:47:35.74	0.331
9:55:34.560	+69:38:23.32	9:55:34.567	+69:38:24.00	0.681
9:55:58.613	+69:40:47.17	9:55:58.553	+69:40:47.25	0.331
Bright SDSS Sources identified in <i>HST</i> ACS/WFC Observations				
SDSS R.A.	SDSS Decl.	<i>HST</i> R.A.	<i>HST</i> Decl.	Displacement (")
9:55:47.134	+69:40:41.87	9:55:47.002	+69:40:41.71	0.727
9:55:41.806	+69:41:15.41	9:55:41.664	+69:41:15.26	0.777
9:55:46.805	+69:40:38.09	9:55:46.656	+69:40:37.99	0.806
9:55:55.711	+69:41:05.42	9:55:55.546	+69:41:05.29	0.901

TABLE 2
HST OBSERVATIONS AND MAGNITUDES OF SEVERAL SOURCES IN THE REGION OF M82 X-1.

Date	Data Set	Instrument/Filter	Exp(s)	A	B	C	D	E	F
				m_{Filter}	m_{Filter}	m_{Filter}	m_{Filter}	m_{Filter}	m_{Filter}
2004-02-09	j8mx19010	ACS/WFC/F658N	700	21.523±0.048	22.139±0.063	23.318±0.109	24.480±0.186	22.808±0.086	20.954±0.037
2004-02-09	j8mx19e9q	ACS/WFC/F814W	120	20.812±0.020	21.161±0.023	20.085±0.014	22.255±0.039	22.717±0.048	...
2005-12-08	j9fb09010	ACS/HRC/F330W	3896	25.890±0.091	27.136±0.161	...	26.234±0.106	...	26.431±0.116
2005-12-08	j9fb09030	ACS/HRC/F658N	400	21.506±0.066	...	21.410±0.063	22.673±0.112	22.404±0.099	21.383±0.062
2006-01-31	j9fb57030	ACS/HRC/F435W	1132	25.593±0.052	25.510±0.050	28.171±0.171	26.308±0.072	26.677±0.086	25.700±0.055
2006-01-31	j9fb57010	ACS/HRC/F550M	840	23.276±0.031	23.495±0.034	22.977±0.027	23.878±0.041	24.450±0.053	24.012±0.043
2006-01-31	j9fb57020	ACS/HRC/F814W	140	21.151±0.025	21.448±0.029	20.214±0.016	21.864±0.035	21.948±0.036	22.256±0.042
2006-03-27	j9l021d6q	ACS/WFC/F435W	450	25.660±0.081	25.340±0.070	26.793±0.137	...	26.189±0.104	26.571±0.124
2006-03-27	j9l022deq	ACS/WFC/F435W	450	25.696±0.083	26.375±0.113	26.572±0.124	...	27.045±0.154	26.050±0.097
2006-03-27	j9l023dmq	ACS/WFC/F435W	450	25.886±0.090	26.461±0.118	26.800±0.137	...	27.045±0.154	27.305±0.174
2006-03-27	j9l024duq	ACS/WFC/F435W	450	25.815±0.087	25.438±0.073	26.938±0.147	...	26.231±0.106	26.209±0.105
2006-03-27	j9l021d8q	ACS/WFC/F555W	340	23.578±0.036	23.891±0.042	23.746±0.039	24.592±0.057	25.603±0.091	...
2006-03-27	j9l022dgq	ACS/WFC/F555W	340	23.792±0.040	23.913±0.042	23.696±0.038	25.414±0.084	25.789±0.099	...
2006-03-27	j9l023doq	ACS/WFC/F555W	340	24.077±0.045	24.112±0.046	24.060±0.045	25.245±0.077	25.366±0.082	...
2006-03-27	j9l024dwq	ACS/WFC/F555W	340	23.779±0.039	23.865±0.041	23.800±0.040	24.888±0.066	25.565±0.090	...
2006-03-27	j9l021daq	ACS/WFC/F658N	1100	22.492±0.059	23.114±0.079	22.620±0.063	23.698±0.103	22.345±0.055	21.114±0.031
2006-03-27	j9l022diq	ACS/WFC/F658N	1100	23.812±0.108	22.231±0.052	21.083±0.031	...	21.851±0.044	21.065±0.031
2006-03-27	j9l023dqq	ACS/WFC/F658N	1100	23.649±0.101	22.487±0.059	21.020±0.030	...	22.688±0.065	21.315±0.034
2006-03-27	j9l024dyq	ACS/WFC/F658N	1100	22.329±0.055	22.938±0.073	20.959±0.029	...	22.425±0.057	21.129±0.032
2006-03-27	j9l021d5q	ACS/WFC/F814W	175	21.068±0.018	21.489±0.022	20.151±0.012	21.528±0.023	22.824±0.041	...
2006-03-27	j9l022ddq	ACS/WFC/F814W	175	21.438±0.022	21.557±0.023	20.456±0.014	22.066±0.029	22.050±0.029	...
2006-03-27	j9l023dlq	ACS/WFC/F814W	175	21.254±0.020	21.665±0.024	20.569±0.015	21.952±0.028	22.428±0.035	...
2006-03-27	j9l024dtq	ACS/WFC/F814W	175	20.882±0.017	21.190±0.020	20.292±0.013	21.339±0.021	22.166±0.031	...
2009-11-17	ib6w81060	WFC3/UVIS/F225W	1070	...	27.031±0.416	27.218±0.453	26.384±0.309
2009-11-17	ib6w81050	WFC3/UVIS/F336W	1050	26.861±0.228	27.352±0.286	...	27.785±0.349	...	27.552±0.314
2009-11-15	ib6w83020	WFC3/UVIS/F373N	2850	25.194±0.196	24.981±0.178	28.094±0.746	25.774±0.257	...	26.383±0.340
2009-11-17	ib6w82030	WFC3/UVIS/F487N	2455	24.142±0.087	25.558±0.167	24.807±0.118	24.652±0.110	25.128±0.137	25.989±0.203
2009-11-17	ib6w82020	WFC3/UVIS/F502N	2465	24.637±0.093	...	25.601±0.144	25.139±0.117
2009-11-17	ib6w81040	WFC3/UVIS/F547M	360	24.072±0.065	23.862±0.059	24.554±0.081	24.220±0.069	25.005±0.100	24.381±0.075
2009-11-15	ib6w83030	WFC3/UVIS/F673N	2760	21.814±0.026	22.068±0.029	21.310±0.020	23.750±0.063	24.034±0.071	23.650±0.060
2010-01-01	ib6wr9030	WFC3/UVIS/F225W	1665	28.206±0.575
2010-01-01	ib6wr9020	WFC3/UVIS/F336W	1620	26.509±0.157	...	26.989±0.195	28.275±0.353	26.280±0.141	27.828±0.287
2010-01-01	ib6wr9010	WFC3/UVIS/F547M	1070	23.244±0.026	23.615±0.030	24.050±0.037	24.884±0.055	25.251±0.065	24.757±0.052